Journal of Hepatocellular Carcinoma

Dovepress
open access to scientific and medical research

Open Access Full Text Article

ORIGINAL RESEARCH

Endoplasmic Reticulum Membrane Protein Complex Regulates Cancer Stem Cells and is Associated with Sorafenib Resistance in Hepatocellular Carcinoma

Yuan-Jie Liu[1,*], Jing-Xiao Li[1,*], Jie-Pin Li[1], Yi-Dou Hu[2], Zhi-Bin Ma[3], Wei Huang[1], Shen-Lin Liu[1], Xi Zou[1]

[1]Affiliated Hospital of Nanjing University of Chinese Medicine, Jiangsu Province Hospital of Chinese Medicine, Nanjing, Jiangsu, 210029, People's Republic of China; [2]Zhangjiagang TCM Hospital Affiliated to Nanjing University of Chinese Medicine, Zhangjiagang, Jiangsu, 215600, People's Republic of China; [3]Nanjing YOUMENG Biology Science and Technology Co. Ltd, Nanjing, Jiangsu, 210029, People's Republic of China

*These authors contributed equally to this work

Correspondence: Xi Zou; Shen-lin Liu, Email fsyy00670@njucm.edu.cn; lsljsszyy@126.com

Background: Hepatocellular carcinoma (HCC) remains a leading cause of cancer-related mortality, underscoring the need for novel therapeutic targets. This study aimed to elucidate the role of endoplasmic reticulum membrane protein complex subunit 1 (EMC1) in HCC progression and its therapeutic potential.

Methods: Publicly available sequencing data and biopsy specimens were analyzed to assess EMC's clinical value and functions in HCC. In vitro experiments validated EMC functions, and multiplex immunofluorescence analysis examined EMC-associated sorafenib resistance mechanisms. EMC1 expression was knocked down in HCC cell lines, followed by cell viability, wound healing, and transwell migration assays. Tumor growth and response to sorafenib treatment were evaluated in mouse models. Metabolomic analysis assessed changes in the TCA cycle.

Results: EMC genes were aberrantly expressed in HCC, and high EMC1 expression correlated with poorer survival rates. EMC1 disruption enhanced HCC cells' sensitivity to sorafenib, reducing cell viability, increasing apoptosis, and decreasing tumor size and weight. EMC1 maintained cancer cell stemness and promoted M2 macrophage infiltration. Metabolomic analysis revealed significant changes in the TCA cycle, indicating EMC1's role in HCC metabolic reprogramming. Importantly, EMC1 is highly associated with sorafenib resistance, potentially linked to CTNNB1 mutation or activation.

Conclusion: EMC1 plays a critical role in regulating the sorafenib resistance in HCC. Targeting EMC1 may improve HCC treatment efficacy.

Keywords: endoplasmic reticulum membrane complex subunit 1, catenin beta 1, tumor stemness, M2 macrophage, sorafenib resistance

Introduction

Hepatocellular carcinoma (HCC), the most common primary hepatic malignancy, is characterized by high recurrence, metastasis, and mortality due to its complex pathophysiology.[1,2] Over half of the global incidence occurs in China, placing a significant burden on the local healthcare system.[3] Sorafenib, a multi-tyrosine kinase inhibitor, remains the standard first-line therapy for advanced-stage HCC.[4] However, the overall response rate to sorafenib is suboptimal due to frequent primary and acquired resistance.[5–7] Advances in immunology and molecular biology have highlighted dysregulation of molecular signaling pathways and immunosuppression as key factors in sorafenib resistance, though the

Received: 17 April 2024
Accepted: 1 August 2024
Published: 9 August 2024

precise mechanisms are not yet fully understood.[8] T Thus, elucidating the mechanisms underlying HCC invasion, metastasis, and sorafenib resistance is crucial for improving patient prognosis.

The endoplasmic reticulum (ER) membrane protein complex (EMC) was first identified in yeast studies as crucial for cellular transmembrane transport.[9,10] EMC is composed of nine proteins arranged around a highly conserved core, notably the EMC3-EMC6 subcomplex.[11] Advances in structural resolution have enhanced our understanding of membrane protein biogenesis across all life forms, revealing that EMC abnormalities are linked to various human diseases.[9,12] In cancer research, EMC6 has emerged as a potential prognostic biomarker for pancreatic, lung, and gastric cancers,[13,14] underscoring the growing recognition of EMC's role in tumors.

However, research on EMC in the context of tumors remains sparse. To address this, a comprehensive analysis of EMC in cancer is crucial. In the present study, we examined the expression heterogeneity of genes encoding 10 EMC subunits across various cancers. Our analysis revealed that genomic alterations, particularly copy number variations (CNVs), impact EMC levels. We specifically investigated the role of EMC in HCC. Through Friends analysis, we identified EMC1—a gene not previously studied in HCC—as significantly associated with the disease.

Further investigations involving single-cell analysis and in vitro experiments demonstrated that EMC1 plays a critical role in maintaining cancer cell stemness and enhancing the tricarboxylic acid (TCA) cycle. Additionally, using multiple immune infiltration algorithms and spatial transcriptome analysis, we established that EMC1 is essential for M2 macrophage infiltration. Multiplex immunofluorescence (mIF) further validated the association of EMC1 with β-catenin and M2 macrophage markers. Consequently, we have delineated the EMC1/cancer stem cells (CSCs)/M2 macrophage axis.

Materials and Methods

Public Datasets and Corresponding Processing

For pan-cancer analyses, we utilized the GSCALite web tool to process data from The Cancer Genome Atlas (TCGA).[15] For hepatocellular carcinoma (HCC) data specifically (TCGA-LIHC), we employed the R package "TCGAbiolinks" to download RNA sequencing data (RNA-seq, FPKM values) and converted these values to Transcripts Per Million (TPM).[16] Pathology image data were obtained from the Genomic Data Commons (GDC) portal.[17] For datasets from the Gene Expression Omnibus (GEO),[18] we assigned each HCC sample an EMC score using single-sample gene set enrichment analysis (ssGSEA) and conducted subsequent analyses using the Biomarker Exploration of Solid Tumors (BEST) database.[19,20] Specifically, for sorafenib resistance data (GSE109211, GSE94550, and GSE73571), we downloaded the raw data via the "GEOquery" package and processed them into expression matrices for further analysis.[21–24] The single-cell RNA sequencing (scRNA-seq) data used in this study (GSE166635) were sourced from a prior HCC study.[25]

scRNA-Seq Data Analyses

The filtered output of Cellranger from hepatocellular carcinoma (HCC) single-cell RNA sequencing (scRNA-seq) data, which included cells from two patients[26], was analyzed in this study. A total of 22,631 cells were processed using Seurat V4.[27] We utilized the uniform manifold approximation and projection (UMAP) coordinates and cell annotation information provided by the Tumor Immune Single Cell Hub (TISCH) without additional processing. Malignant cells were then distinguished from epithelial cells. The "FindAllMarkers" function with default parameters was employed to identify markers for each malignant cluster[28], and dot plots were generated using the "Nebulosa" package.[29]

To analyze communication between malignant and myeloid cells, we utilized the ligand-receptor information from the "CellChat" package.[30] Additionally, cell stemness and metabolism scores were calculated using the "CytoTRACE" and "scMetabolism" packages, respectively.[31,32]

Spatial Transcriptome (ST) Analysis

We downloaded spatially resolved transcriptomics data sets VISDS000514 and VISDS000511 from the CROST database, a comprehensive repository for spatial transcriptomics.[33] M2 macrophage scores for each spot were assessed

using the xCell method, while EMC+ epithelial cell scores were determined using single-sample gene set enrichment analysis (ssGSEA).[34] The spatial overlap of EMC+ epithelial cells, M2 macrophages, and macrophage migration inhibitory factor (MIF) was visualized using the "SpatialPlot" function in Seurat V4.

Estimation of Immunological Characteristics in the Tumor Microenvironment (TME) of HCC

To analyze the correlation between EMC levels and immune profiles, we utilized the BEST database and visualized the results with heatmaps.

Calculation of the Stemness Level of Malignant Cells

In TCGA-LIHC, we calculated the mRNA-based stem index (mRNAsi) value (ranging from 0 to 1) for each HCC sample, which was strongly correlated with the characterization of the level of dedifferentiation, with higher values representing stronger stemness. Further, the correlation between the mRNAsi index and EMC1 was analyzed.

Enrichment Analysis

Gene Ontology (GO) and Kyoto Encyclopedia of Genes and Genomes (KEGG) enrichment analyses for EMC were conducted using the BEST web tool.[35,36] Additionally, Metascape was employed to compare signaling differences among various clusters of malignant cells.[37]

Reagents

All employed antibodies and reagents are listed in Table S1.

Cell Culture

Human HCC HuH-7 and SK-Hep1 cells were obtained from Wuhan Pu-nuo-sai Life Technology Co. Ltd. Hepa1-6-luc cell obtained from Cellcook Biotech Co., Ltd. Sorafenib-resistant hepatoma cell lines (Huh7 sorafenib-resistant cells and SK-Hep1 sorafenib-resistant cells) were acquired from Shanghai Zhong Qiao Xin Zhou Biotechnology Co., Ltd. Cells were cultured in Dulbecco's Modified Eagle Medium (DMEM) with 10% FBS at 37°C in a 5% CO_2 humid incubator. Sorafenib was added to the cell lines (Huh-7/Sorafenib and SK-Hep1/Sorafenib) at a concentration of 2 μg/mL to maintain resistance as per the manufacturer's instructions. THP-1 cells (human monocytic cells) were purchased from the cell bank of the Chinese Academy of Sciences (Shanghai, China). THP-1 cells were cultured in Roswell Park Memorial Institute-1640 (RPMI-1640) medium supplemented with 10% fetal bovine serum (FBS) in incubator at 37°C in 5% CO_2.

Lentiviral Vector Generation and Cell Transfection

Lentiviral vectors were employed for EMC1 knockdown experiments. The GeneChem Corporation synthesized the viruses. The specific information is shown in Table S2. For transient transfection, cells were transfected according to the manufacturer's indications. In short, HCC cells underwent a 24-hour recombinant lentiviral transduction via 2 μg/mL polybrene, and the successfully transfected cells were screened with 1.5 μg/mL puromycin. Lastly, Western blot assays were used to determine EMC1 knockdown efficiencies as well as outcomes.

Western Blotting (WB)

In a previous report, the WB protocol was described.[38] Proteins were extracted from lysed cells using radioimmunoprecipitation (RIPA) buffer, followed by Bradford assays. Subsequently, sodium dodecyl-sulphate polyacrylamide gel electrophoresis (SDS-PAGE) was conducted with either a 10% or 8% gel concentration to obtain 20 μg of each sample. The samples were then transferred onto a polyvinylidene fluoride (PVDF) membrane. Subsequently, the membrane was blocked using a 5% bovine serum albumin (BSA) solution. Following this, primary antibodies were incubated with the membrane overnight at 4°C. The membrane was then washed three times with an incubation solution containing Tris-

buffered saline and 0.05% Tween-20. Subsequently, the membrane was labeled using secondary antibodies. The β-actin were utilized as references.

CCK8 Assay

We evaluated the IC_{50} of HCC using the CCK8 assay. We put 5×10^3 HCC cells in 96-well plates and cultured them with 5% CO_2 at 37 °C for 24 hours. The cells were then treated with sorafenib in culture medium for another 24 hours. Optical density (OD) was then measured at 450 nm using a microplate reader (BioTek Synergy HT).

Animal Experiments

For the subcutaneous xenograft tumor model, 36 male BALB/c nude mice (6 weeks of age) were randomly divided into six groups. Huh-7 and Huh7 sorafenib-resistant cells (Huh7/sorafenib) were infected with/without NC or sh-EMC1 for 24 hours, then collected for subcutaneous injection (1×10^6 cells/injection) into athymic BALB/c nude mice. Once the subcutaneous nodules grew to the size of a rice grain (approximately one week), the subcutaneous xenograft model was successfully established. The nude mice were then treated with sorafenib by gavage at a dosage of 30 mg/kg/day for 21 days. On day 28, the mice were euthanized, and subcutaneous tumor tissues were harvested for further analysis. Tumors were excised, fixed in 10% formalin, and embedded in paraffin.

For the orthotopic liver tumor model, Hepa1-6-luc cells were infected with/without NC or sh-EMC1 for 24 hours, then collected for injection (5 × 10^5 cells/injection). Eighteen male 6-week-old C57BL/6 mice were divided into three groups: control group, NC group, and sh-EMC1 group. Mice were anesthetized using isoflurane (oxygen delivered at 0.5 L/min with 3% isoflurane for induction and 1.5% isoflurane for maintenance). After sterilizing the site, a 2 mm transverse incision was made below the xiphoid, perpendicular to the median line, and was 1–1.5 cm long. The left liver lobes were carefully pulled out of the abdominal cavity with a sterile cotton swab. A 0.2 cm incision was made in Glisson's capsule to serve as the transplantation site. The cells were directly inoculated into the left liver lobe of the mice through a 27-gauge needle. To prevent tumor cell leakage from the injection point, a gelatin sponge patch, 2 mm in diameter, was attached to the site of injection for a few minutes after needle withdrawal.Seven days after Hepa1-6-luc cell inoculation, the mice were administered sorafenib orally at a dose of 30 mg/kg/day for 21 days. On day 28, the mice were anesthetized and intraperitoneally injected with 1.5 mg D-Luciferin in 100 μL PBS for the live imaging assay. The fluorescence images were analyzed using AniView SE Living Imaging software (BLT, Guangzhou, China). All mice were sacrificed 28 days after Hepa1-6-luc cell inoculation, and the tumors were fixed for further experiments. Additionally, to account for potential variations in tumor size, we calculated a "tumor ratio" as the percentage of tumor area to the entire liver for each mouse. This study adhered to the COPE guidelines and complied with ARRIVE guidelines 2.0 (https://arriveguidelines.org/arrive-guidelines). All animal experimental procedures were conducted in accordance with the Basel Declaration and were approved by the Animal Ethics Committee of Jiangsu Province Hospital of Chinese Medicine (Ethics approval number: 2022DW-10-01).

Hematoxylin and Eosin (HE) Staining

The histopathology of liver tissues was evaluated using HE staining. After dehydration in an ethanol gradient, liver samples were embedded in paraffin and sectioned into 4-μm pieces following immersion in a 10% formaldehyde solution. The sections were then deparaffinized, stained with hematoxylin and eosin, mounted, and examined under an upright epifluorescent microscope (Nikon, Eclipse Ni-E, Japan).

Patient's Specimens and Clinical Data Collection

Primary liver cancer tissues and adjacent non-tumor samples were collected from 80 patients with HCC at the Affiliated Hospital of Nanjing University of Chinese Medicine. Tumors were selected based on the criterion that no prior chemotherapy or radiation therapy had been administered before surgical resection. Upon extraction, tissue specimens were rinsed with cold phosphate-buffered saline, fixed immediately in 4% paraformaldehyde, and subsequently embedded in paraffin. Histopathological examination confirmed the diagnosis of HCC in all patients following hepatectomy. Informed consent was obtained from each patient participating in this study. Additionally, clinical data

were retrieved from the electronic medical records of the same hospital. This study was conducted in accordance with ethical standards and received approval from the Ethics Committee of the Affiliated Hospital of Nanjing University of Chinese Medicine (Ethics approval number: 2022NL-162-02). Table S3 shows the clinical and pathological data of patients.

Immunohistochemical (IHC) and Immunofluorescence (IF) Staining

The protocols for IHC and IF staining were adopted from previous investigations.[39,40] The final concentrations of antibodies were established based on previous studies or as recommended by the antibody providers. Tissue sections were first blocked with a protein blocking solution to minimize non-specific binding. Following this, the slides were incubated with the primary antibody. Immunohistochemical (IHC) scoring, which evaluated both staining intensity and extent, was performed independently by two researchers. Images were captured using a NIKON Eclipse Ni-E microscope (NIKON, Japan). Staining intensity was classified as follows: 0 for negative, 1 for weak, 2 for moderate, and 3 for strong. The extent of staining was assessed based on the percentage of positively stained cells: 0 for no positive staining, 1 for less than 10% positive staining, 2 for 10–50% positive staining, and 3 for more than 50% positive staining. The overall IHC score, or H-SCORE, was computed by combining the staining intensity and the proportion of stained cells, using the formula: H-SCORE = $\sum$(PI × I) = (percentage of cells with weak intensity × 1) + (percentage of cells with moderate intensity × 2) + (percentage of cells with strong intensity × 3). In this context, PI denoted the percentage of positively stained cells relative to the total number of cells in a specified field of view, while I represented the intensity of staining. The H-SCORE ranged from 0 to 300, with a higher value indicating a more pronounced positive staining.

Tissue sections or cell climbing slides were first subjected to blocking with either 5% bovine serum albumin (BSA) in phosphate-buffered saline (PBS) or 0.1% Tween-20 to reduce non-specific binding. Following blocking, the slides were incubated overnight at 4 °C with the primary antibody. After this, the slides were treated with secondary antibodies at 25 °C for 1 hour. Nuclear staining was performed using 4',6-diamidino-2-phenylindole (DAPI) for 3 minutes in the dark. The slides were then rinsed four times with PBS for 5 minutes each. Finally, the sections were sealed with an immunofluorescence quencher solution. Immunofluorescence staining was observed, and images were captured using an inverted fluorescence microscope (Olympus CKX-4, Japan).

Sphere Production

To evaluate sphere formation capabilities, 5×10^3 HCC cells were seeded per well in 6-well ultralow attachment plates. The cells were incubated for 7 days in serum-free medium supplemented with 20 ng/mL human recombinant fibroblast growth factor (FGF), 20 ng/mL human recombinant epidermal growth factor (EGF), and 2% B27. The number and size of the formed spheres were subsequently analyzed using light microscopy (Olympus BX53, Japan).

Colony Formation Assays

We seeded 500 HCC cells per well in 6-well plates and incubated them for approximately 14 days. Following incubation, colonies were stained with 0.5% crystal violet at room temperature (20–25°C) for 10 minutes. Colony formation was then assessed and counted using a stereomicroscope (Nikon, MZ1500, Japan).

Transwell Assay

To assess the invasive ability of the cells, a Transwell invasion assay was conducted. In 24-well Transwell chambers, the upper compartment was filled with 200 μL of DMEM medium, and 1×10^4 cells were seeded. The lower compartment was supplemented with 500 μL of medium containing 10% FBS as a chemoattractant. A layer of Matrigel was applied to the upper compartment to simulate the extracellular matrix. After a 24-hour incubation period, the upper compartment was washed with 1% PBS. Cells were then fixed with 4% paraformaldehyde for 15 minutes and stained with 0.1% crystal violet. For analysis, cells were photographed in 5 random fields under a light microscope (Olympus BX53, Japan) and counted.

Wound Healing Assay

The migratory ability of HCC cell lines was evaluated using a wound healing assay. In each well of six-well plates, 4×10^5 cells were seeded and incubated for 24 hours in serum-free medium. Following incubation, the medium was removed, and wounds were created in the cell monolayer using a 200-μL pipette tip. The rate of wound closure was assessed at three time points (0, 24, and 48 hours) using an Olympus CKX-41 inverted microscope with a 200× magnification.

Transmission Electron Microscopy (TEM)

The morphology of mitochondria was examined using transmission electron microscopy (TEM). Cells were prepared according to the manufacturer's protocol. Specimens were stained with 0.3% lead citrate and observed under an electron microscope (Hitachi, Tokyo, Japan) at magnifications of 2500× or 30,000×.

Measurement of ATP Content

HCC cells were seeded at a density of 2×10^5 cells per well in six-well plates. After 24 hours of incubation, the growth medium was replaced with 0.1 mL of glucose- and FBS-free DMEM, and cells were further incubated for 12 hours. ATP levels were measured using an ATP assay kit. Cells were lysed and centrifuged at 12,000 × g for 5 minutes. In a 96-well plate, 100 μL of cell lysate was mixed with 100 μL of ATP detection working solution. ATP levels were quantified using the BioTek Synergy HT Microplate Reader. Protein concentration in the lysates was determined using a BCA assay kit. The ATP level was calculated by normalizing the ATP concentration to the total protein concentration (ATP level = ATP concentration / total protein concentration).

Establishment of a Co-Culture System

To induce macrophage differentiation, THP-1 cells (1×10^5 cells/mL) were cultured in 6-well plates and treated with phorbol 12-myristate 13-acetate (PMA) for 24 hours.[41] The PMA-containing medium was replaced with serum-free medium and the cells were cultured for another day. Two days prior to the co-culture experiment, cells (1×10^5 cells/mL) from the control group, knock-down group (sh-EMC1), and negative control (NC) group were seeded onto 0.4-μM transwell inserts. For co-culture, the culture medium in the inserts with HCC cells was removed to the top of the 6-well plates with differentiated THP-1 cells (macrophage). The cells were co-cultured for an additional 48 hours, and macrophage were harvested for immunofluorescence staining.

Enzyme Linked Immunosorbent Assay (ELISA)

Considering that Macrophage migration inhibitory factor (MIF) is a secreted protein, its concentration within the co-culture system was assessed utilizing the MIF ELISA Kit. The supernatant was carefully transferred from the culture into sterile vessels, followed by a 20-minute centrifugation at 2000 rpm to isolate the supernatant. The ELISA assay was conducted in adherence to the manufacturer's instructions, with the optical density of each well measured at 450 nm using a Bio-Tek Synergy HT microplate reader immediately thereafter.

Retrospective Study

This retrospective study included 20 patients with HCC who received sorafenib monotherapy following transarterial chemoembolization (TACE) at the Affiliated Hospital of Nanjing University of Chinese Medicine from March 2022 to March 2024. All patients were pathologically diagnosed through hepatic aspiration biopsy. Lesion samples from the biopsies were evaluated by experienced pathologists in the Department of Pathology. The patient clinicopathological characteristics are summarized in Table S4. Inclusion Criteria: Patients were eligible if they: (1) had a confirmed diagnosis of HCC; (2) had a Barcelona Clinic Liver Cancer (BCLC) stage B or C; (3) had good liver function, classified as Child-Pugh scores A to B7; and (4) had an Eastern Cooperative Oncology Group (ECOG) performance status of ≤ 2. Extrahepatic metastases were permitted. Exclusion Criteria: Exclusion criteria were: (1) liver transplantation at any time; (2) presence of only nodal or distant metastases without viable liver lesions; (3) secondary malignancies; (4) prior or

concurrent use of other targeted agents, chemotherapy, or immunotherapy; and (5) serious adverse reactions or drug allergies.

Treatment and Monitoring: Patients were treated with sorafenib starting at 400 mg twice daily (b.i.d). Dose adjustments were made based on toxicity, with a minimum dose of 200 mg b.i.d. on alternate days. The study protocol was approved by the ethics committee of the Affiliated Hospital of Nanjing University of Chinese Medicine (Ethics approval number: 2022NL-162-02), and written informed consent was obtained from all participants. Assessment and Response Evaluation: Radiological assessments were conducted every two months during treatment using liver computed tomography (CT) or magnetic resonance imaging (MRI), based on the Response Evaluation Criteria in Solid Tumors version 1.1. Tumor response was classified as stable if there was no significant change. Non-response was indicated by tumor progression greater than 30% over three consecutive months or evidence of extensive metastases.

Statistical Analysis

The potential relationships between variables were determined using Spearman correlation coefficient. The *t*-test (normally distributed data) and Wilcoxon rank-sum test (non-normally distributed data) were used for two group comparison. Additionally, Kruskal–Wallis and one-way analysis of variance (ANOVA) were employed for within-group and multiple-group comparisons. A two-tailed P-value of 0.05 was used as the significance criterion for all data analyses.

Results

The Transcriptional Variations and Genetic Characteristics of 10 EMC Molecules

Information on the 10 EMC subunit-coding genes was obtained from the HUGO Gene Nomenclature Committee (HGNC) web tool. These genes include *EMC1, EMC2, EMC3, EMC4, MMGT1, EMC6, EMC7, EMC8, EMC9*, and *EMC10* (Table S5). Previous studies have highlighted functional differences of EMC molecules across various cancers. For instance, overexpression of *EMC6* in gastric cancer cells has been shown to inhibit cell growth, migration, and invasion, while knockdown of EMC3 in melanoma has led to enhanced immune responses.[14,42] Thus, EMC molecules may exhibit either cancer-promoting or cancer-inhibiting functions depending on the specific environment. To examine the transcriptional variation of EMC molecules in cancer, we analyzed HCC tissue samples from the TCGA-LIHC cohort alongside normal tissues from both TCGA-LIHC and GTEx databases. As illustrated in Figure S1A, most EMC molecules were upregulated in cancer samples compared to normal controls, suggesting that EMC function may be activated in cancer.

To elucidate the cause of abnormal EMC expression, we analyzed genetic variations, including single nucleotide variants (SNVs) and copy number variations (CNVs), in pan-cancer data. We observed that EMC1 was mutated at a high frequency, particularly in endometrioid cancer (UCEC, 37%), colon cancer (COAD, 13%), skin cutaneous melanoma (SKCM, 10%), and stomach adenocarcinoma (STAD, 10%) (Figure S1B). Among 342 samples with at least one mutation in the 10 EMC genes within TCGA pan-cancer data, EMC1 exhibited the highest mutation frequency (36%), followed by EMC2 (21%) and EMC7 (12%), with missense mutations being the most prevalent. UCEC was the most frequently mutated cancer type (Figure S1C). These findings suggest that aberrant EMC expression may be linked to SNVs, particularly in EMC1.

Next, we investigated the impact of CNVs on EMC expression in pan-cancer datasets. Analysis of CNV frequency revealed substantial variability in the CNV of the 10 EMC genes across different cancers. EMC2 and EMC10 displayed the highest CNV frequencies (Figure S1D), primarily involving copy number heterozygous amplification and deletion (Figure S1E and F). We hypothesize that CNVs, in addition to SNVs, may contribute to the transcriptional dysregulation of EMC molecules. Correlation analysis between CNV and mRNA levels confirmed this hypothesis, showing a positive correlation between CNV and mRNA levels in most cancer types (Figure S1G).

In this study, we focused on the role of EMC in HCC. To accurately compare the differential expression of EMC molecules in various tissue samples, we analyzed paired mRNA expression data from HCC tumor and normal samples. Consistent with earlier findings, we confirmed that all EMC genes were expressed at higher levels in HCC tumor tissues

compared to normal tissues (Figure 1A). Additionally, a high degree of transcriptional correlation among the EMC molecules was observed (Figure 1B). To further explore the expression patterns of EMC molecules in tumor versus normal samples, we performed principal component analysis (PCA). As shown in Figure 1C, principal components PC1, PC2, and PC3 effectively distinguished between normal and tumor samples in the TCGA-LIHC and GTEx datasets. Notably, paracancerous tissue samples (TCGA-LIHC) were more similar to HCC tissue samples than to normal liver tissue samples (GTEx). This suggests that EMC activation may precede malignant transformation in normal tissues. Finally, Cox regression analysis indicated that most EMC genes were associated with adverse outcomes in HCC (Figure 1D, HR > 1). These results suggest that dysregulation of EMC molecules may contribute to the development and progression of HCC.

EMC is Activated in HCC and Associated with Poor Prognostic Features

Next, we examined the clinical and biological significance of EMC in HCC. To achieve this, we constructed an EMC score using the ssGSEA algorithm across nine publicly available datasets, which allowed us to comprehensively evaluate EMC activity (Figure 2A). We classified samples into high and low EMC groups based on the median EMC level. Consistent with the pancancer analysis, the EMC score was significantly elevated in tumor tissues across multiple datasets (E_TABM_36, GSE144269, GSE14520, and TCGA-LIHC) (Figure 2B). Additionally, patients in the high-EMC group exhibited significantly poorer outcomes compared to those in the low-EMC group. This included overall survival (OS) in TCGA-LIHC and GSE144269, progression-free survival (PFS) in TCGA-LIHC, disease-specific survival (DSS) in TCGA-LIHC, disease-free survival (DFS) in TCGA-LIHC, and recurrence-free survival (RFS) in E_TABM_36

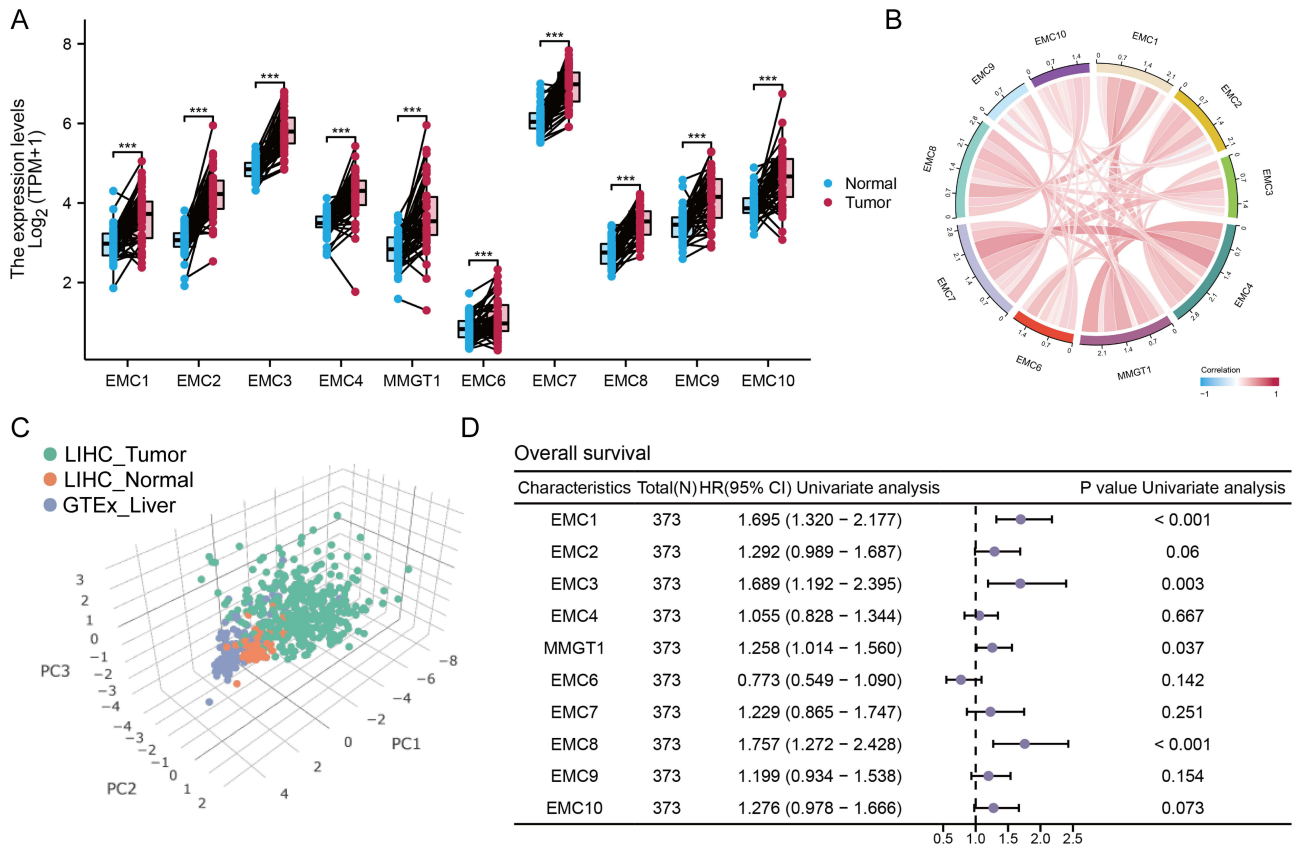

Figure 1 Abnormal patterns of the endoplasmic reticulum (ER) membrane protein complex (EMC) subunits expression in cancer. (**A**) Differential expression of EMC-related molecules between paired normal and cancer samples in TCGA-liver hepatocellular carcinoma (LIHC) (paired *t*-test). (**B**) The chord diagram demonstrates the correlation among EMC-related molecules (TCGA-LIHC). Red color represents positive correlation. (**C**) The three-dimensional map (principal component analysis) was provided to classify the normal liver samples (GTEx) and normal and tumor samples in TCGA-LIHC based on EMC-related molecules. (**D**) The Cox regression analysis of the average OS rate of 10 EMC-related molecules in the TCGA-LIHC cohort. ***P < 0.001.

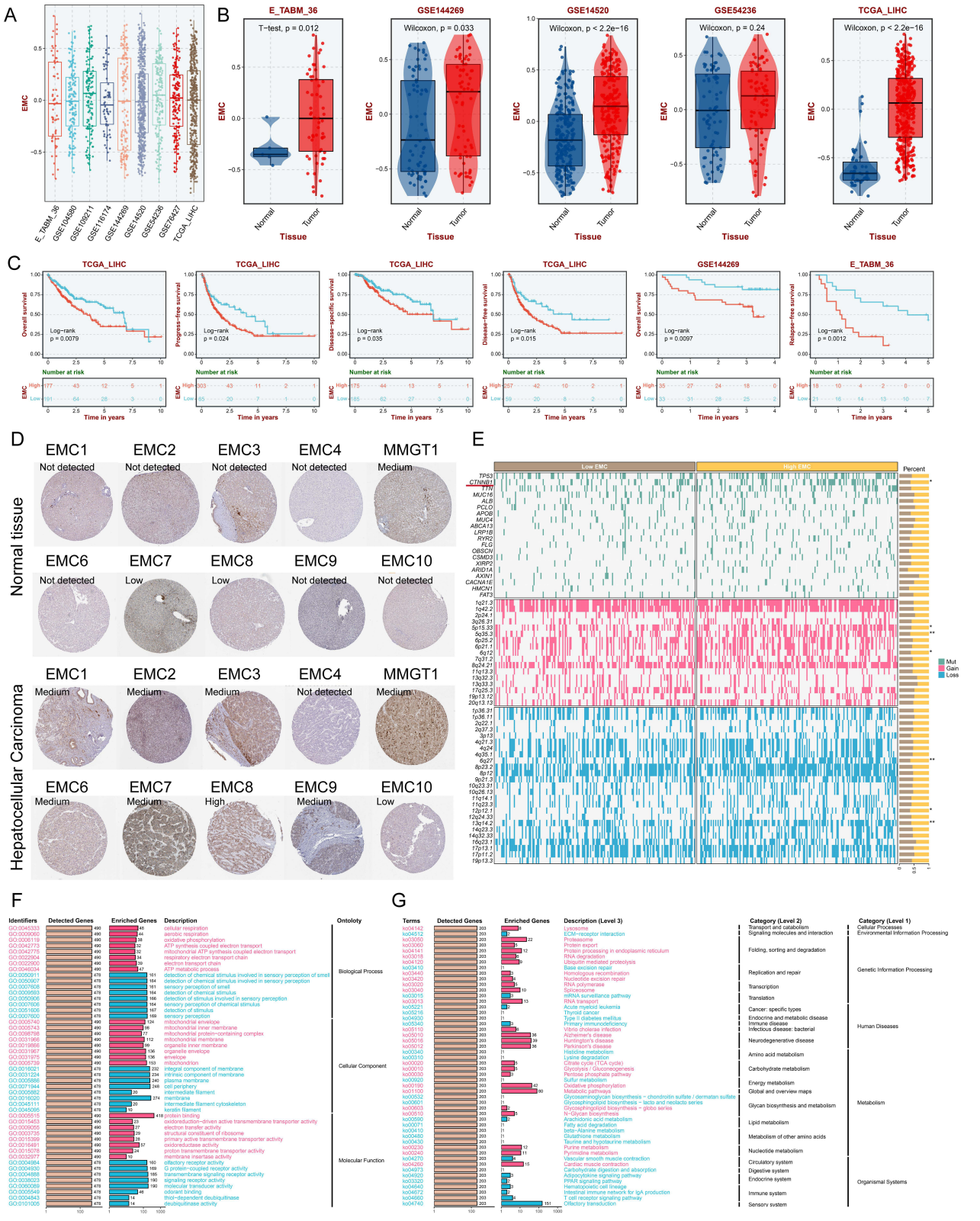

Figure 2 Single sample gene set enrichment analysis (ssGSEA) of EMC. (**A**) The box plots show the EMC levels measured by ssGSEA across the nine publicly available hepatocellular carcinoma (HCC) datasets. (**B**) Differences of EMC levels between cancer samples and normal controls in five public HCC datasets. (**C**) Kaplan-Meier survival curves of OS (TCGA-LIHC and GSE144269), PFS (TCGA-LIHC), DSS (TCGA-LIHC), DFS (disease-free survival, TCGA-LIHC), and RFS (release-free survival, E_TABM_36) analyses according to the median expression level of EMC were generated. (**D**) The representative immunohistochemical (IHC) staining images of EMC subunits in normal and HCC tissues from the online Human Protein Atlas (HPA) database. (**E**) The Oncoplot displays the differences of mutation and CNV profiles between EMC-high and -low groups (cutoff value: median expression level of EMC). (**F** and **G**) Gene ontology (GO, (**F**)) and Kyoto Encyclopedia of Genes and Genomes (KEGG), (**G**) enrichment analysis of EMC. *P < 0.05, **P < 0.01.

(Figure 2C). Moreover, data from the Human Protein Atlas (HPA) database corroborated these findings, showing that the protein levels of EMC subunits were upregulated in HCC tissues (Figure 2D). Pathological examination further revealed that samples with high EMC1 expression exhibited more pronounced cytologic atypia compared to those with low EMC1 expression (Figure S2), indicating a higher degree of malignancy in the former.

We then explored the potential role of EMC in carcinogenesis. Analyzing mutational landscapes and copy number variations in the high- and low-EMC groups using the TCGA-LIHC cohort revealed that the high-EMC group exhibited a higher proportion of mutations, gains, and losses compared to the low-EMC group (Figure 2E). Notably, CTNNB1 mutations were significantly more frequent in the high-EMC group ($P < 0.05$). Given that CTNNB1 mutations lead to aberrant β-catenin expression—a major downstream effector of the Wnt pathway associated with poorer overall survival (OS) in various cancers[43]—this finding underscores the relevance of the β-catenin pathway in EMC-associated tumorigenesis. To further elucidate the functional implications of EMC, we performed biological process (BP) enrichment analysis, which indicated that EMC is primarily involved in cellular respiration, aerobic respiration, oxidative phosphorylation, and ATP synthesis coupled with electron transport. Cellular component (CC) enrichment analysis revealed that EMC's role in tumorigenesis is associated with the mitochondrial envelope, mitochondrial inner membrane, mitochondrial protein-containing complex, and mitochondrial membrane. Molecular function (MF) enrichment analysis highlighted that EMC is enriched in protein binding, oxidoreduction-driven active transmembrane transporter activity, electron transfer activity, and structural constituent of ribosomes (Figure 2F). Additionally, KEGG pathway analysis identified that EMC is involved in several pathways, including oxidative phosphorylation, metabolic pathways, and lysosomes (Figure 2G). These findings suggest that EMC may play a significant role in tumorigenesis through its involvement in key cellular processes and pathways.

EMC Drives β-Catenin Expression and is Associated with Sorafenib Resistance

CTNNB1 mutations are recognized as aberrations associated with acquired drug resistance to several chemotherapeutic agents, including enzalutamide, platinum, and sorafenib.[44–46] To explore this further, we investigated the sensitivity to chemotherapeutic drugs across different EMC levels using the Genomics of Drug Sensitivity in Cancer (GDSC) database. Our analysis revealed a positive correlation between EMC levels and the 50% inhibitory concentration (IC50) values for 30 drugs, including semagacestat, sorafenib, and nilotinib (Figure 3A). Given the significant clinical role of sorafenib in

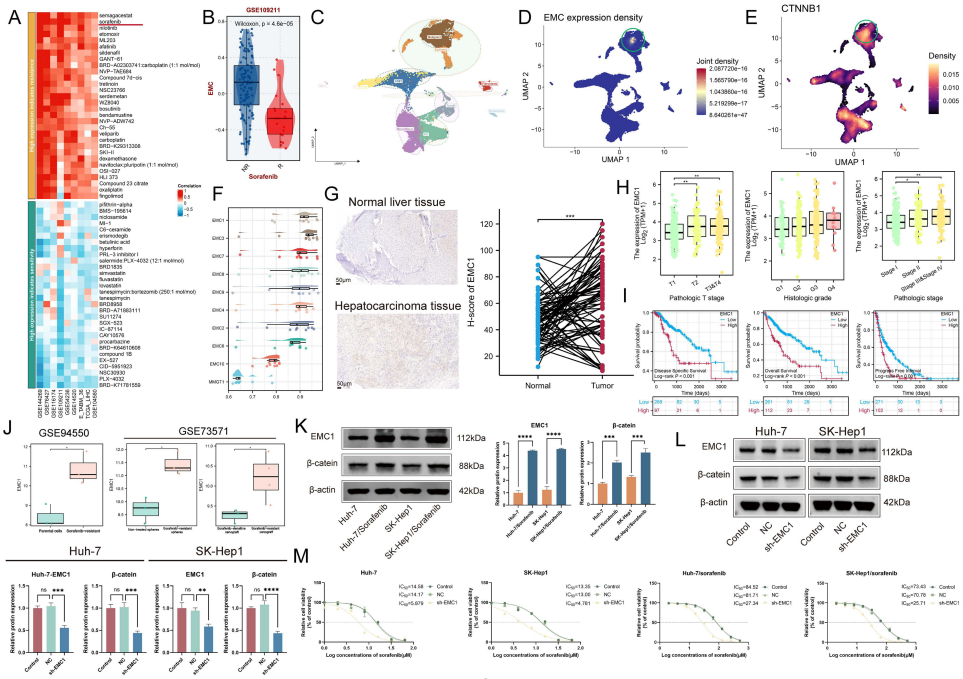

Figure 3 Continued.

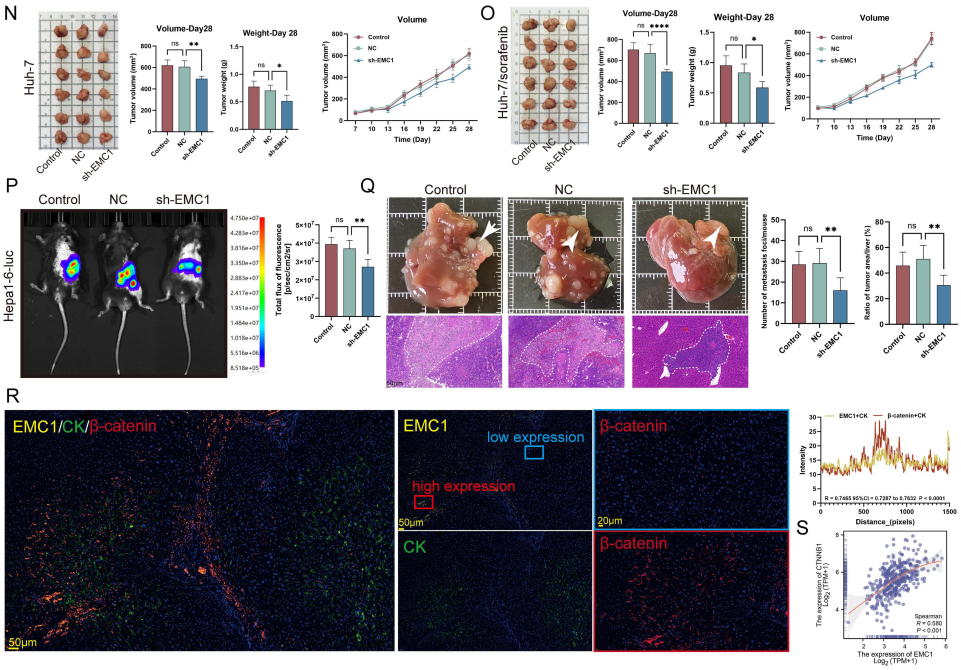

Figure 3 Resistance-related analysis of EMC. (**A**) The heatmap shows the correlations between estimated IC50 values of 60 representative drugs and EMC levels. Sorafenib is highlighted by the red line. (**B**) The boxplot shows the differences in EMC levels between sorafenib-responder (**R**) and non-responder (NR) groups. (**C**) The Uniform Manifold Approximation and Projection (UMAP) graph shows the cell types identified in the single-cell RNA-seq (scRNA-seq) dataset GSE166635. (**D**) UMAP revealing the joint level of EMC genes assessed by "Nebulosa" package. Higher level is indicated with a redder color. (**E**) UMAP revealing the expression level of *CTNNB1*. Higher level is indicated with a lighter color. (**F**) Friends analysis of EMC-related molecules. EMC1 was identified as the key member. (**G**) IHC staining of our own samples for analyzing EMC1 expression in HCC versus normal liver tissues. Wilcoxon rank sum test. (**H**) The expression level of *EMC1* among different pathologic T stages, histological grades, and pathologic stages was analyzed in TCGA-LIHC. Kruskal–Wallis Test. (**I**) DSS, OS, and progression-free interval (PFI) analyses according to the medium expression level of the *EMC1* gene were performed using HCC cases in the TCGA-LIHC cohort. (**J**) Box plots of *EMC1* expression in parental cells and sorafenib-resistant cells (GSE94550), non-treated spheres and sorafenib-resistant spheres (GSE73571), and sorafenib-sensitive xenograft and sorafenib-resistant xenograft (GSE73571). Wilcoxon rank sum test. (**K**) Western blot for confirming the differential protein levels of EMC1 between sorafenib-resistant cell lines and controls (Huh-7 and SK-Hep). *T* test. (**L**) Western blot of β-catenin in EMC1-disrupted Huh-7 and SK-Hep cells. *T* test. (**M**) Dose-response curves of HCC treated with sorafenib. The IC50 values for the control, NC, and sh-EMC1 groups. Each data point represents the mean ± SD of three independent experiments. Knockdown of EMC1 significantly increased the sensitivity of both HCC cell lines (Huh-7 and SK-Hep1) and sorafenib-resistant cells (Huh-7/sorafenib and SK-Hep1/sorafenib) to sorafenib treatment, as evidenced by the lower IC50 values in the sh-EMC1 groups compared to the NC groups. (**N** and **O**) Representative images of tumors harvested from Huh-7 (**N**) and Huh-7/ sorafenib (**O**) xenografts in BALB/c nude mice treated with sorafenib for 21 days. Tumors from control, NC, and sh-EMC1 groups are shown. Tumor volume and weight analysis at day 28 post-inoculation. Tumor volumes (left) were measured over time, and the tumor weights (right) were recorded at the end of the study. Knockdown of EMC1 significantly reduced tumor volume and weight compared to NC groups (ANOVA). (**P**) Representative bioluminescence images of mice with Hepa1-6-luc orthotopic liver tumors. Mice were divided into three groups: Control, NC, and sh-EMC1. The bioluminescence signal, indicative of tumor burden, was measured 28 days post-inoculation. Quantification of the total flux of bioluminescence (p/sec/cm²/sr) in the different groups. The sh-EMC1 group showed a significant reduction in bioluminescence signal compared to the NC groups. (**Q**) Representative images of livers harvested from the control, NC, and sh-EMC1 groups showing visible metastatic foci (indicated by white arrowheads). HE staining of liver sections from the control, NC, and sh-EMC1 groups. Dashed lines outline the metastatic regions. Scale bar = 50 μm. Quantification of the number of metastatic foci per mouse and Ratio of tumor area to total liver area (%) in the control, NC, and sh-EMC1 groups. The sh-EMC1 group showed a significant reduction in tumor area ratio compared to the NC groups. (**R**) Multiple immunofluorescence (mIF) staining images of EMC1, β-catenin, and CK in the HCC biopsy. Scale bar, 50 μM; nuclei (DAPI) in blue. A representative view of co-staining was shown in the enlarged images at right (scale bar, 20 μM). Co-localization (EMC1+CK versus β-catenin+CK) was quantified using the Spearman correlation coefficient (n = 80). (**S**) Spearman correlation between *EMC1* and *CTNNB1* in TCGA-LIHC. The experiment was repeated three times. ns, not significant, *P < 0.05, **P < 0.01, ***P < 0.001, ****P < 0.0001.

treating HCC, we focused specifically on its relationship with EMC. Further validation in the GSE109211 dataset showed that EMC levels were significantly higher in the sorafenib non-responder group compared to the responder group (Figure 3B). Additionally, we observed that EMC was highly expressed in malignant cells (Figure 3C and D and Figure S3), where CTNNB1 expression was also upregulated (Figure 3E). These findings suggest that EMC may contribute to sorafenib resistance through CTNNB1-related signaling pathways.

To further investigate the molecular mechanisms of EMC, we performed an analysis using Friends to identify the most critical EMC members. As depicted in Figure 3F, EMC1 emerged as the most strongly correlated with other EMC subunits, suggesting it plays a pivotal role in EMC-related biological signaling. The protein-protein interaction (PPI) network analysis also identified EMC1 as a potential hub gene (Figure S4, red circle). Consequently, we focused on EMC1 for further investigation.

We assessed EMC1 expression in 80 pairs of HCC and adjacent non-cancerous tissues using immunohistochemistry (IHC). The results revealed a significant upregulation of EMC1 in HCC tissues (Figure 3G). Clinical analysis indicated

that EMC1 expression positively correlated with T stage, tumor grade, and pathological stage. Survival analysis demonstrated that overall survival (OS), disease-specific survival (DSS), and progression-free interval (PFI) were significantly reduced in HCC patients with high EMC1 expression compared to those with low EMC1 expression (Figure 3H and I, TCGA-LIHC). These findings underscore the importance of EMC1 in HCC.

We then investigated the association between EMC1 and sorafenib resistance. As shown in Figure 3J, EMC1 was significantly upregulated in drug-resistant cell lines (GSE94550), drug-resistant spheres (GSE73571), and drug-resistant xenograft tumors (GSE73571), suggesting a strong correlation between EMC1 and secondary sorafenib resistance. For in vitro validation, we compared EMC1 protein levels between resistant and non-resistant cell lines. We found that EMC1 protein expression was elevated in sorafenib-resistant Huh-7 and SK-Hep1 cell lines (Figure 3K).

We then transfected HCC cells with sh-EMC1 and confirmed the transfection efficiency (Figure 3L). Western blot analysis showed that sh-EMC1 reduced intracellular β-catenin levels (Figure 3L), indicating that EMC1 regulates β-catenin expression. Additionally, CCK-8 assays revealed a significant decrease in the IC50 value of sorafenib in both parent and drug-resistant Huh-7 and SK-Hep1 cells treated with sh-EMC1 (Figure 3M). These results suggest that targeting EMC1 may enhance sorafenib sensitivity in HCC.

To investigate the role of EMC1 in sorafenib resistance in vivo, we established both xenograft and orthotopic transplantation models. EMC1-disrupted or control cells were subcutaneously injected into BALB/c nude mice using Huh-7 and Huh-7-SR cell lines, or orthotopically transplanted into C57BL/6 mice using the Hepa1-6-luc cell line. The mice were subsequently treated with sorafenib. Our results demonstrated that knockdown of EMC1 enhanced sensitivity to sorafenib, as evidenced by reduced tumor sizes and areas at the endpoint analysis (Figure 3N–Q).

To further validate the association between EMC1 and β-catenin, we performed multiplex immunofluorescence (mIF) on HCC tissues. The analysis revealed strong expression of β-catenin in regions with high EMC1 expression and minimal β-catenin expression in areas with low EMC1 levels (Figure 3R; EMC1+CK versus β-catenin+CK, R = 0.7465). This correlation was also supported by bulk data from TCGA-LIHC (R = 0.580, Figure 3S). In conclusion, our findings indicate that EMC1 mediates resistance to sorafenib in HCC cells.

Down-Regulation of EMC1 Impairs HCC Cell Stemness and Inhibits the Tricarboxylic Acid (TCA) Cycle

Given that EMC was upregulated in malignant cells, we conducted a clustering analysis of all malignant cells to explore the precise role of EMC. As shown in Figure 4A, the "FindClusters" function identified three distinct cell subgroups (malignant C1-C3). Differentially expressed gene (DEG) analysis highlighted the top 5 genes with high and low expression levels in these subgroups (Figure 4B and Table S6). Enrichment analysis revealed that malignant C1 and C2 were associated with a broader array of cancer-related signaling pathways compared to malignant C3, suggesting that C3 may be less malignant (Figure 4C). Notably, malignant C1 exhibited strong correlations with KRAS signaling, adipogenesis, angiogenesis, mTORC1 signaling, and xenobiotic metabolism—pathways not prominently observed in C2 and C3.

CytoTRACE analysis, which assesses dedifferentiation and stemness properties, showed that malignant C1 and C2 had significantly higher CytoTRACE scores than C3 (Figure 4D). This suggests that C1 and C2 may represent potential cancer stem cell (CSC) populations, further supported by their low levels of epithelial markers (Figure 4E, EPCAM +CDH1+KRT18). Additionally, EMC1 was upregulated in malignant C1 and C2, indicating its potential role in maintaining HCC cell stemness (Figure 4F). Bulk data also showed a weak positive correlation between EMC1 transcript levels and tumor stemness (Figure 4G, R = 0.12).

To further investigate the impact of EMC1 on stemness characteristics, we performed in vitro experiments. Sphere formation assays demonstrated that downregulation of EMC1 impaired cancer cell stemness and reduced sphere formation in Huh-7 and SK-Hep1 cells (Figure 4H). Moreover, clone formation (Figure 4I), wound healing (Figure 4J), and transwell migration (Figure 4K) assays revealed that EMC1 interference significantly inhibited cell proliferation, migration, and invasion.

There is evidence that β-catenin deficiency leads to mitochondrial dysfunction in hepatocytes, including impaired tricarboxylic acid (TCA) cycle activity and oxidative phosphorylation (OXPHOS), ultimately resulting in reduced adenosine triphosphate (ATP) production.[47] Tumor cells often exhibit impaired TCA cycle function and rely primarily on glycolysis for ATP

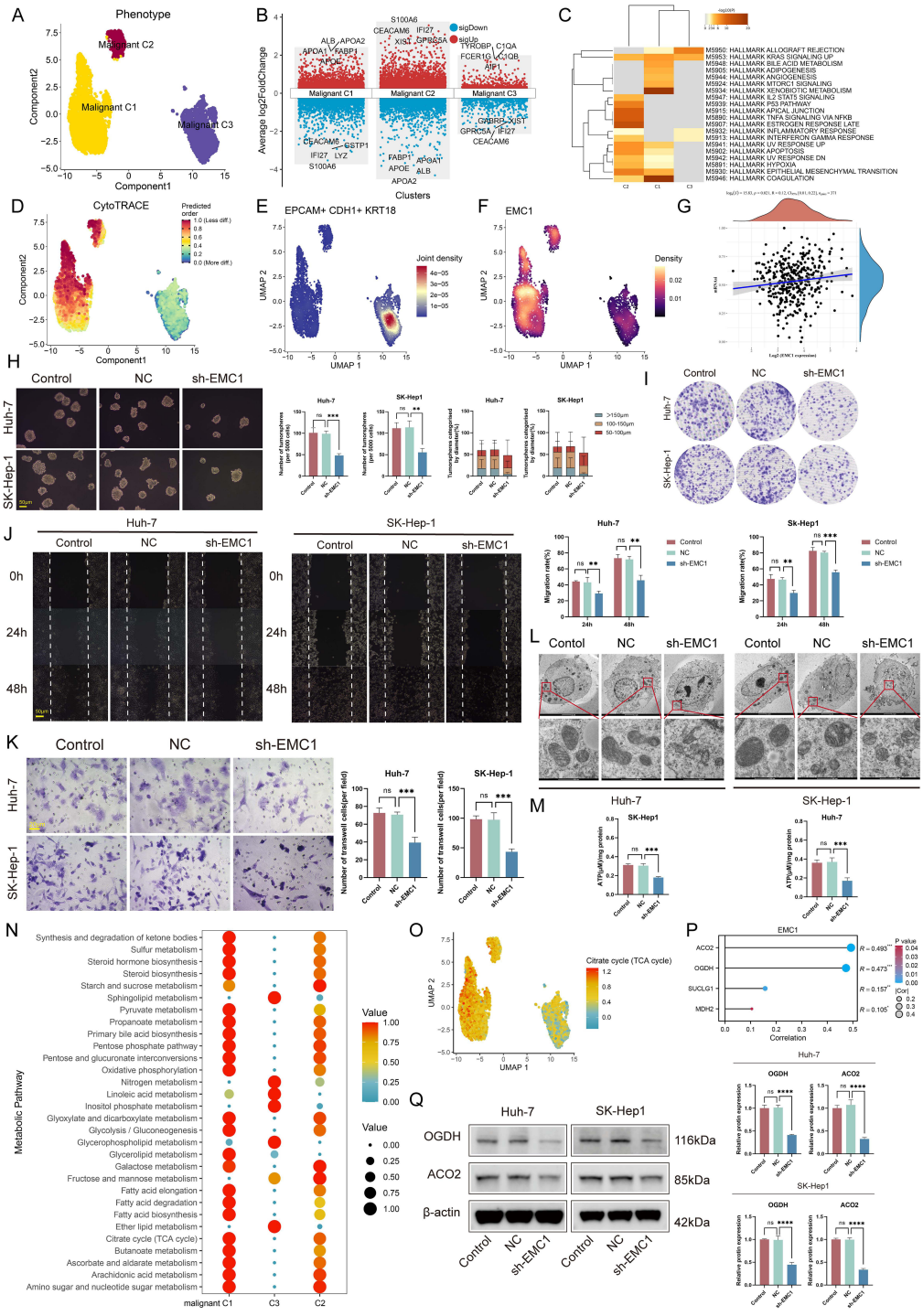

Figure 4 Downregulation of EMC impairs cancer stem cell (CSC) phenotype and inhibits the tricarboxylic acid (TCA) cycle. (**A**) Malignant cell populations were re-clustered into three subclusters (color coding). (**B**) Differential gene analysis of three malignant cell clusters (malignant C1, C2, and C3). The top five upregulated (red) and downregulated (blue) genes was shown. (**C**) GO and KEGG enrichment analysis of the three malignant cell clusters. (**D**) UMAP revealing the stemness level of malignant cells assessed by "CytoTRACE" package. Higher level is indicated with a redder color. (**E**) UMAP revealing the joint level of epithelial marker (*EPCAM, CDH1*, and *KRT18*). Higher level is indicated with a redder color. (**F**) UMAP revealing the expression level of *EMC1*. Higher level is indicated with a lighter color. (**G**) Spearman correlation between EMC1 and the stemness index (mRNAsi) in TCGA-LIHC. (**H**) 3D sphere-formation assays in sh-EMC1 Huh-7 and SK-Hep-1 cells. Scale bars, 50μm. (**I–K**) Colony formation (**I**), wound-healing (**J**), and transwell migration (**K**) assays in EMC1-disrupted Huh-7 and SK-Hep-1 cells. Scale bar for J, 50 μm; Scale bar for K, 20 μm. (**L**) Ultrastructures of mitochondria (sh-EMC1 Huh-7 and SK-Hep-1 cells) were observed by transmission electron microscope (TEM). (**M**) Bar plots show the changes in ATP after sh-EMC1 treatment. (**N**) The bubble plot demonstrates the metabolic differences between different malignant clusters. (**O**) UMAP revealing the levels of TCA cycle in different malignant clusters. Higher level is indicated with a redder color. (**P**) Spearman correlation between EMC1 and the key enzymes of TCA cycle (TCGA-LIHC). (**Q**) Western blot of the two most relevant enzymes in EMC1-disrupted Huh-7 and SK-Hep cells. *T* test. The experiment was repeated three times. *P < 0.05, **P < 0.01, ***P < 0.001, ****P < 0.0001.

Abbreviation: ns, not significant.

production. However, they still depend on mitochondria-associated reductive carboxylation to metabolize glutamine.[48,49] Mitochondria-endoplasmic reticulum interactions are crucial for regulating mitochondrial respiration and bioenergetics in cancer cells.[50] This prompted us to investigate whether downregulation of EMC1 could influence mitochondrial structure and function.

Transmission electron microscopy revealed that sh-EMC1 treatment impaired mitochondrial structure (Figure 4L), and suppression of EMC1 resulted in reduced ATP production in HCC cells (Figure 4M). We then assessed the metabolic profiles of each malignant subpopulation using the "scMetabolism" package and visualized the scores for the top 30 metabolic pathways. The levels of glycolysis, pyruvate metabolism, oxidative phosphorylation, lipid metabolism (eg, steroid biosynthesis), and the TCA cycle were notably higher in malignant C1 compared to other malignant clusters (Figure 4N), consistent with the characteristics of CSCs.

Focusing on the TCA cycle (Figure 4O), we found a significant positive correlation between EMC1 levels and the transcript levels of two TCA enzymes: Aconitase 2 (*ACO2*, R = 0.493) and Oxoglutarate Dehydrogenase (*OGDH*, R = 0.473) (Figure 4P, TCGA-LIHC). Western blotting further confirmed that downregulation of EMC1 resulted in decreased expression of ACO2 and OGDH in Huh-7 and SK-Hep1 cells (Figure 4Q). These findings suggest that EMC1 regulates mitochondrial metabolic pathways in HCC cells.

EMC1 Promotes M2 Macrophage Phenotype

CSCs interact with the immune system, thereby promoting immune evasion.[51] In this study, we further explored the potential oncogenic mechanisms of EMC1 through alterations in the immune microenvironment. Initially, we employed eight immune estimation algorithms to assess the association between EMC and immune cell infiltration. As illustrated in Figures 5A and S5, there is a notable correlation between EMC levels and the abundance of M2 macrophages (highlighted in the red box). Subsequently, we conducted a co-expression analysis using HCC datasets to determine the correlations between EMC levels and immunomodulator-related genes. The heatmap (Figure 5B and Figure S5) clearly shows that β2-Microglobulin (*B2M*) and C-C Motif Chemokine Ligand 15 (*CCL15*) are co-expressed with EMC (highlighted in the red box). Both B2M and CCL15 have been widely demonstrated to induce M2-like polarization of macrophages. To further investigate, we performed cell communication analyses to study the interactions between EMC-represented CSC populations and myeloid cells. Our findings suggest that malignant C1 cells may interact more intensively with myeloid cells compared to other malignant groups (Figure 5C). Further ligand-receptor analyses indicated that malignant C1 cells may frequently communicate with myeloid cells through MIF signaling, leading to phenotypic changes in these cells (Figure 5D, highlighted in the red box). Numerous studies have emphasized the role of MIF signaling in the TME, particularly in suppressing innate immunity.[52] Our analysis also identified that SPP1 signaling predominantly originates from malignant C1 cells (Figure 5E and F). To validate the cellchat analysis results, we obtained spatial transcriptional data from the CROST database to characterize the spatial overlap of EMC+ epithelial cells, M2 macrophages, and MIF signaling within HCC cancer tissues. Consistently, a portion of EMC+ epithelial cells, M2 macrophages, and MIF were found to be concentrated at the same locations (Figure 5G–I), indicating their physical proximity. To examine whether EMC1 contributes to the maintenance of the M2-like phenotype of macrophages in vitro, we established a co-culture model as depicted in Figure 5J. After 48 hours of co-culture with sh-EMC1-treated HCC cells, macrophages exhibited a reduced M2-like profile (Figure 5K, indicated by decreased CD163 expression). Additionally, ELISA analysis of the co-cultures showed that MIF secretion levels in the sh-EMC1 group were significantly lower than those in the control/NC group (Figure 5L). For in vivo validation, we performed IHC on the aforementioned transplant tumors. As shown in Figure 5M, sh-EMC1 treatment significantly reduced CD163 expression levels. Multiplex immunofluorescence (mIF) staining of HCC tissue samples further demonstrated that the infiltration level of M2 macrophages near tumor tissues with high EMC1 expression was also higher (Figure 5N; EMC1+CK versus CD163, R = 0.9441). In conclusion, EMC1 appears to help maintain the M2-like phenotype of macrophages through MIF signaling.

The Expression of EMC1 and CTNNB1 is Positively Correlated with CD163 Activity in Human HCC Patients

We further examined the correlation between EMC1, CTNNB1, CD163 activity, and sorafenib resistance. In the TCGA-LIHC dataset, we observed positive correlations between *EMC1, CTNNB1*, and *CD163* (Figure 6A). Interestingly, this

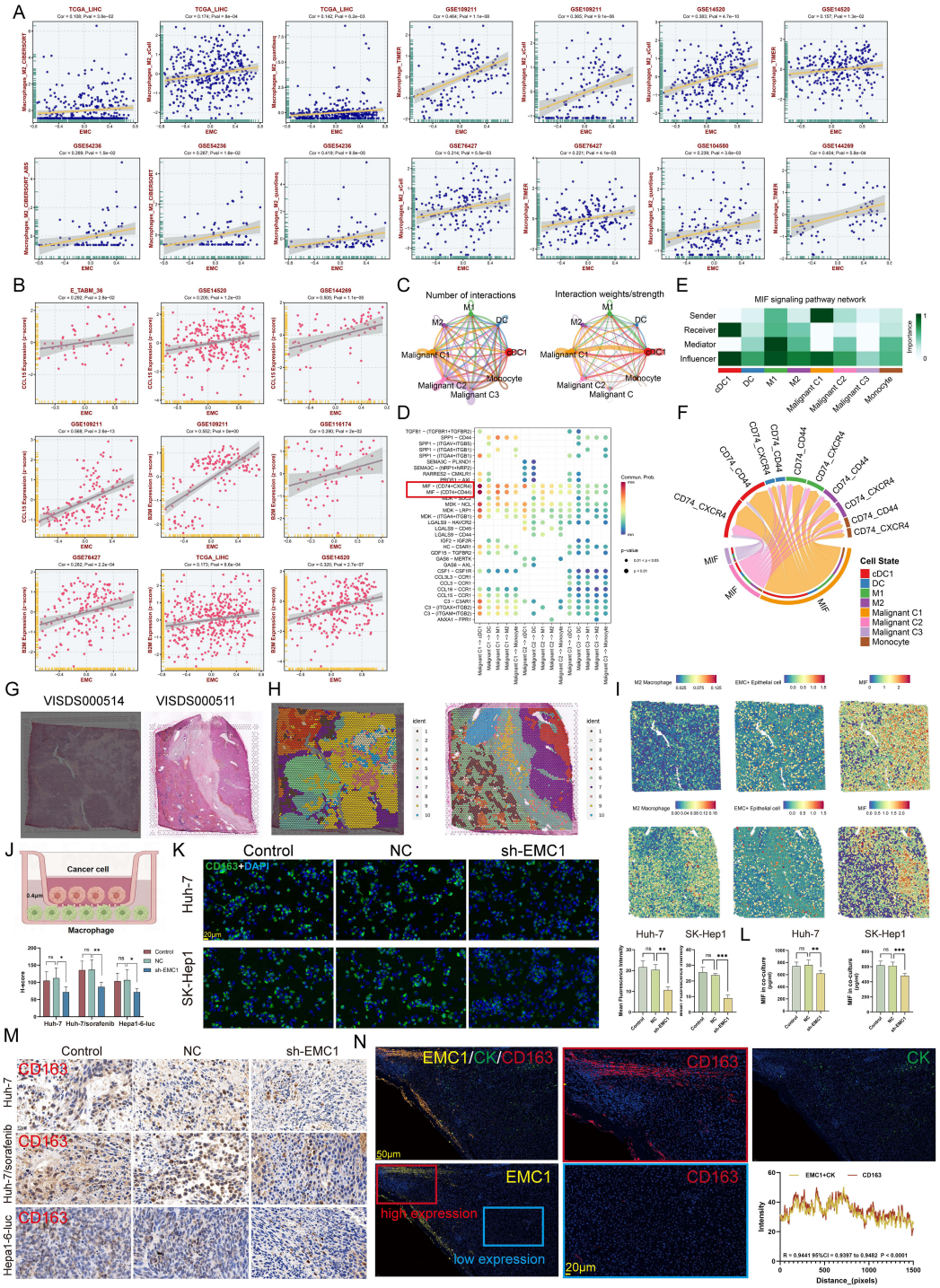

Figure 5 EMC1 promotes M2 macrophage phenotype through MIF. (**A**) Scatter plots show the correlation between EMC (ssGSEA) and M2 macrophages estimated by multiple algorithms. (**B**) Scatter plots show the correlation between EMC (ssGSEA) and C-C Motif Chemokine Ligand 15 (*CCL15*) as well as Beta-2-Microglobulin (*B2M*). (**C**) The circle plots show the number (left) or strength (right) of interactions in the cell-cell communication network. (**D**) The bubble plot shows that malignant C1 may communicate with myeloid cell frequently through MIF signals (red box). (**E** and **F**) The heatmap (**E**) and chord diagram (**F**) demonstrate that malignant C1 is the major sender of MIF signaling. (**G**) Hematoxylin and eosin (H&E) staining of tissue sections of ST spots in HCC samples VISDS000514 (left) and VISDS000511 (right). (**H**) Unbiased clustering of ST spots in HCC samples VISDS000514 (above) and VISDS000511 (below). (**I**) Spatial overlap of signature score of M2 macrophages, EMC+ Epithelial cells, and MIF in tissue sections. (**J**) Co-culture model diagram of cancer cells (above) and macrophages (below). (**K**) IF staining of M2 marker CD163 in macrophages with the intervention of EMC1-disrupted Huh-7 and SK-Hep cells. *T* test. (**L**) Enzyme-linked immunosorbent assay (ELISA) of MIF in the co-culture system. (**M**) Representative IHC images showing CD163 expression in Huh-7, Huh-7/sorafenib, and Hepa1-6-luc mouse model tumor tissues. The control, NC, and sh-EMC1 groups are displayed for each cell line. Brown staining indicates CD163 expression, while blue staining represents the nuclei. Scale bar = 10 μm. Quantitative analysis of CD163 expression levels in mouse model tumor tissues, demonstrating a significant reduction in CD163expression in the sh-EMC1 group compared to the NC groups. Data are presented as H-scores (mean ± SD) for each group. (**N**) mIF staining images of EMC1, CK, and CD163 in the HCC sections. Scale bar, 50 μM; nuclei (DAPI) in blue. A representative view of co-staining was shown in the enlarged images at right (scale bar, 20 μM). Co-localization (EMC1+CK versus CD163) was quantified using the Spearman correlation coefficient (n = 80). *P < 0.05, **P < 0.01, ***P < 0.001.
Abbreviation: ns, not significant.

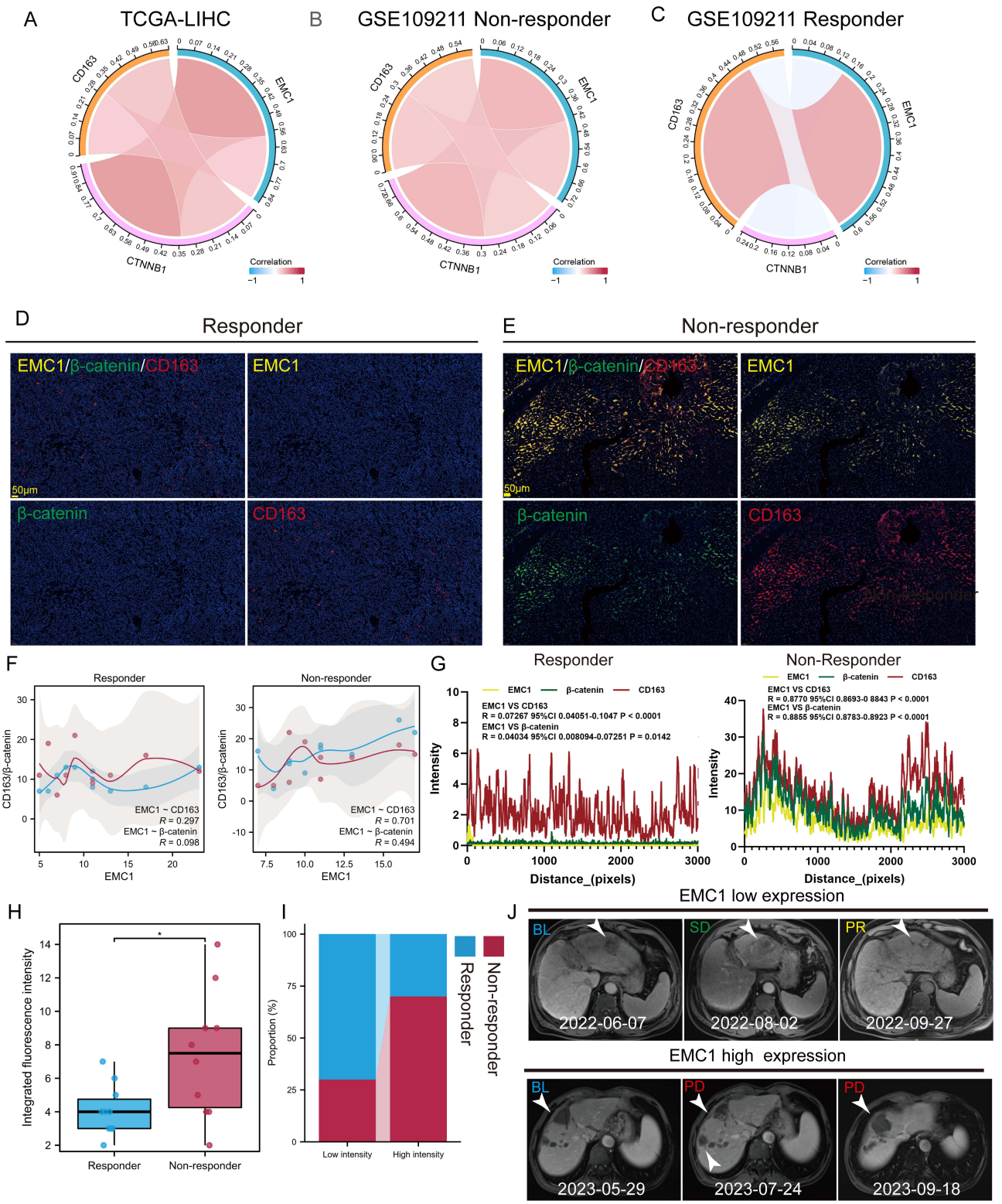

Figure 6 The expressions of EMC1, β-catenin, and CD163 are positively correlated in Sorafenib-resistant HCC samples. (**A**–**C**) Circle plots show the Spearman correlation among *EMC1, CTNNB1*, and *CD163* in TCGA-LIHC (**A**), GSE109211 non-responder samples (**B**), and GSE109211 responder samples (**C**). Red represents positive correlation and blue represents negative correlation. (**D** and **E**) mIF staining images of EMC1, β-catenin, and CD163 in the HCC sections from responder (**D**) and non-responder human donors. Scale bar, 50 μM; nuclei (DAPI) in blue. (**F**) EMC1 co-localizes with β-catenin and CD163 in non-responders. Co-localization was quantified using the Spearman correlation coefficient. (**G**) EMC1 levels are positively correlated with β-catenin and CD163 levels in non-responders. (**H**) Box plot showing distinct Integrated fluorescence intensity (between responder and non-responder after sorafenib therapy in 20 HCC patients. (**I**) Bar plot showing distinct response rates between the high- and low-intensity groups in 20 HCC patients. (**J**) Representative imaging of patients with HCC in EMC1 low- and high-groups. *P < 0.05.

Abbreviation: BL: baseline. SD: stable disease, PR: partial response, PD: progressive disease.

positive correlation persisted in the non-responder group of the GSE109211 dataset, while it disappeared in the responder group (Figure 6B and C). To verify this phenomenon, we performed multiplex immunofluorescence (mIF) staining of EMC1, CTNNB1, and CD163 in 80 cases of human primary HCC. As shown in Figure 6D and E, the subjects were divided into two groups based on their response to sorafenib: non-responders and responders (see Methodology section for details). The results indicated a strong positive correlation between the expression of EMC1, CTNNB1, and CD163 in the non-responder group, whereas no significant correlation was observed in the responder group (Figure 6F). Additionally, the degree of co-localization of these three markers was higher in the non-responder group compared to the responder group (Figure 6G). We also examined the correlation between the combined expression levels of these markers and the response to sorafenib treatment. The integrated expression levels (EMC1 and CTNNB1 expression in CK-positive regions and overall CD163 expression) were lower in responder patients than in non-responders (Figure 6H). Patients with high integrated expression levels had lower response rates to sorafenib than those with low integrated expression levels (Figure 6I). Figure 6J demonstrates the imaging of representative lesions.In conclusion, the positive correlation between EMC1, CTNNB1, and CD163, particularly in non-responders, suggests that their combined expression may be associated with sorafenib resistance in HCC.

Discussion

The endoplasmic reticulum membrane protein complex (EMC) plays a crucial role in the insertion of transmembrane domains (TMDs) into lipid bilayers, thereby regulating the folding and assembly of membrane proteins.[53,54] Membrane proteins are integral to various biological processes, including transmembrane signaling and substance transport, due to their ubiquitous presence in biological membranes.[55] Under normal physiological conditions, protein processing in the ER is tightly regulated. However, in pathological states such as tumors, an adverse microenvironment driven by metabolic and transcriptional abnormalities can disrupt ER homeostasis, thereby promoting malignancy.[56,57] In this study, we explored the genetic and transcriptional diversity of 10 EMC subunits using a pan-cancer database. We found that aberrant activation of EMC may be linked to copy number variations. Further analysis of HCC cases from multiple independent datasets revealed that EMC levels were significantly elevated in tumor tissues and correlated with poor prognosis. Notably, genomic data indicated an association between EMC and CTNNB1 mutations. CTNNB1 mutations are known to activate the Wnt/β-catenin signaling pathway, which, in conjunction with other oncogenic signals, can enhance tumor growth.[58,59]

Wnt/β-catenin signaling plays a pivotal role in the pathophysiological changes in the liver.[60] It has been demonstrated that upstream signaling mechanisms help maintain the stemness of HCC cells and promote an invasive phenotype through the activation of β-catenin.[61] Importantly, CSCs exhibit self-renewal capabilities and mediate drug resistance through enhanced DNA repair mechanisms.[62] For patients with advanced HCC, sorafenib is a effective treatment option and is used as first-line therapy.[63,64] However, CSCs in HCC are resistant to sorafenib, which can contribute to secondary resistance.[65] Our findings indicate that EMC1 is highly expressed in drug-resistant HCC samples and plays a role in maintaining the stemness of HCC cells, thus promoting an aggressive phenotype. Due to the inherent heterogeneity of tumors, it is proposed that CSCs may utilize a distinct metabolic program compared to bulk tumor cells. Under hypoxic conditions, the flow of glucose through the TCA cycle is reduced while glycolytic enzymes are upregulated, a phenomenon known as the Warburg effect. This adaptation helps cancer cells cope with hypoxia.[66] Recent evidence, however, suggests that certain cancer cells with specific transcriptional profiles may rely on the TCA cycle for energy production, particularly during metastasis.[67] Our results support this hypothesis and highlight that EMC may drive CSCs to preferentially oxidize glucose in the mitochondria. Notably, EMT and CSC-like features are critical factors in cancer cell metastasis. CSCs not only drive metastasis but also stimulate angiogenesis to facilitate the spread of cancer.[68,69]

Uncovering the intricate interactions between various cells in the TME and reversing tumor-mediated immunosuppression are foundational elements of current immunotherapies.[70] CSCs respond to multiple upstream signals by secreting cytokines that promote M2-like macrophage activity.[71] In the present study, using ssGSEA, we found a significant positive correlation between EMC levels and M2 macrophage infiltration abundance. Integration of cell communication analysis with spatial transcriptomics revealed frequent interactions between EMC+ epithelial cells and myeloid cells, with close spatial proximity to M2 macrophages. It is suggested that CSCs produce high levels of MIF,

which amplifies the activity of M2 macrophages.[72] Our in vitro and in vivo results support the hypothesis that EMC maintains M2 macrophage infiltration in HCC tissues through MIF. Recent studies highlight the crucial role of M2 macrophages in acquired drug resistance, with targeting these cells potentially reversing therapy resistance.[73] For instance, paclitaxel resistance has been associated with increased M2 macrophages, which protect cancer cells from chemotherapy-induced cell death.[74,75] In HCC, M2 macrophage polarization-mediated sorafenib resistance has also been observed, linking this mechanism to stem cell generation.[76] These consistent findings suggest that EMC may facilitate CSC-M2 macrophage crosstalk in the TME of sorafenib-resistant patients, establishing a positive feedback loop that may contribute to immunosuppression through chemokine secretion. Further in-depth studies are needed to validate this mechanism and elucidate the complete role of EMC in modulating the response to sorafenib in HCC patients.

This study has some limitations. Firstly, while we used multiple bioinformatics algorithms to infer tumor infiltration components, we may have overlooked immune cell types not assessed by these algorithms but relevant to the TME. Secondly, although our data indicate a significant role of EMC1 in sorafenib resistance, the functions of other EMC subunits, particularly EMC3, remain unexplored. Our group is conducting further research in this area.[77] Lastly, treatments such as TACE or other perturbations may alter the TME composition.[77] High-dose localized chemotherapy can disrupt the microenvironment balance, provoke inflammatory responses, activate antitumor immunity, and affect tumor vascularization and metabolism,[78] potentially introducing bias. Additional studies are required to isolate the effects of sorafenib monotherapy from the influence of prior TACE treatment.

Conclusion

Our study revealed novel prognostic mechanisms involving EMC in the HCC population, particularly highlighting its association with CSCs and M2 macrophages. The EMC/CSCs/M2 macrophage axis appears to negatively impact responsiveness to sorafenib treatment. Further research into EMC-related genes could uncover new therapeutic targets for HCC.

Data Sharing Statement

We declare that all the data in this article are authentic, valid, and available for use on reasonable request.

Ethics Approval and Consent to Participate

The study's protocol was approved by the ethics committee of Affiliated Hospital of Nanjing University of Chinese Medicine, and informed consent was obtained from clinicians and patients (approval number: 2022NL-162-02). The study was in accordance with the declaration of Helsinki.

Consent for Publication

Prior to the commencement of data collection, the first author obtained written consent from all participants concerning participation and subsequent publication of the study results. Informed consent to publish personal data was obtained from the patients and/or their legal guardians.

Acknowledgment

The authors would like to express the gratitude to Mr. Zhang Qian for his generosity in this study.

Author Contributions

All authors made a significant contribution to the work reported, whether that is in the conception, study design, execution, acquisition of data, analysis and interpretation, or in all these areas; took part in drafting, revising or critically reviewing the article; gave final approval of the version to be published; have agreed on the journal to which the article has been submitted; and agree to be accountable for all aspects of the work.

Funding

The present study was supported by Jiangsu Provincial Medical Key Laboratory (ZDXYS202208-2), Jiangsu Province Hospital of Chinese Medicine Peak Academic Talent Project (y2021rc19), Science and Technology Project of Affiliated Hospital of Nanjing University of Chinese Medicine (Y2020CX62), Jiangsu Provincial Health and Medical Committee Key Projects (ZD2022070), Jiangsu Province Postgraduate Research Innovation Program Project (KYCX23-2169), Natural Science Foundation of China (82205212), and the personal fees from Mr. Zhang Qian.

Disclosure

The authors declare no conflicts of interest in this work.

References

1. Forner A, Reig M, Bruix J. Hepatocellular carcinoma. *Lancet*. 2018;391(10127):1301–1314. doi:10.1016/S0140-6736(18)30010-2
2. Wen N, Cai Y, Li F, et al. The clinical management of hepatocellular carcinoma worldwide: a concise review and comparison of current guidelines: 2022 update. *Biosci Trends*. 2022;16(1):20–30. doi:10.5582/bst.2022.01061
3. Xu XF, Xing H, Han J, et al. Risk Factors, Patterns, and Outcomes of Late Recurrence After Liver Resection for Hepatocellular Carcinoma: a Multicenter Study From China. *JAMA Surg*. 2019;154(3):209–217. doi:10.1001/jamasurg.2018.4334
4. Yau T, Park JW, Finn RS, et al. Nivolumab versus sorafenib in advanced hepatocellular carcinoma (CheckMate 459): a randomised, multicentre, open-label, Phase 3 trial. *Lancet Oncol*. 2022;23(1):77–90. doi:10.1016/S1470-2045(21)00604-5
5. Xia S, Pan Y, Liang Y, Xu J, Cai X. The microenvironmental and metabolic aspects of sorafenib resistance in hepatocellular carcinoma. *EBioMedicine*. 2020;51:102610. doi:10.1016/j.ebiom.2019.102610
6. Wu J, Chai H, Li F, Ren Q, Gu Y. SETD1A augments sorafenib primary resistance via activating YAP in hepatocellular carcinoma. *Life Sci*. 2020;260:118406. doi:10.1016/j.lfs.2020.118406
7. Yousef EH, El-Magd NFA, El Gayar AM. El Gayar, Norcantharidin potentiates sorafenib antitumor activity in hepatocellular carcinoma rat model through inhibiting IL-6/STAT3 pathway. *Transl Res*. 2023;260:69–82. doi:10.1016/j.trsl.2023.05.005
8. Tian X, Yan T, Liu F. Link of sorafenib resistance with the tumor microenvironment in hepatocellular carcinoma: mechanistic insights. *Front Pharmacol*. 2022;13:991052. doi:10.3389/fphar.2022.991052
9. Zhu Q, Zhu X, Zhang L. ER membrane complex (EMC): structure, functions, and roles in diseases. *FASEB j*. 2024;38(6):e23539. doi:10.1096/fj.202302266R
10. Chitwood PJ, Hegde RS. The Role of EMC during Membrane Protein Biogenesis. *Trends Cell Biol*. 2019;29(5):371–384. doi:10.1016/j.tcb.2019.01.007
11. Pleiner T, Tomaleri GP, Januszyk K, Inglis AJ, Hazu M, Voorhees RM. Structural basis for membrane insertion by the human ER membrane protein complex. *Science*. 2020;369(6502):433–436. doi:10.1126/science.abb5008
12. Volkmar N, Thezenas ML, Louie SM, et al. The ER membrane protein complex promotes biogenesis of sterol-related enzymes maintaining cholesterol homeostasis. *J Cell Sci*. 2019;132(2). doi:10.1242/jcs.223453
13. Zhou X, Xiao B, Jiang M, Rui J. Pan-cancer analysis identifies EMC6 as a potential target for lung adenocarcinoma. *iScience*. 2024;27(1):108648. doi:10.1016/j.isci.2023.108648
14. Wang X, Xia Y, Xu C, Lin X, Xue P, Zhu S. ER membrane protein complex subunit 6 (EMC6) is a novel tumor suppressor in gastric cancer. *BMB Rep*. 2017;50(8):411–416. doi:10.5483/BMBRep.2017.50.8.065
15. Alam MS, Rahaman MM, Sultana A, Wang G, Mollah MNH. Statistics and network-based approaches to identify molecular mechanisms that drive the progression of breast cancer. *Comput Biol Med*. 2022;145:105508. doi:10.1016/j.compbiomed.2022.105508
16. Colaprico A, Silva TC, Olsen C, et al. TCGAbiolinks: an R/Bioconductor package for integrative analysis of TCGA data. *Nucleic Acids Res*. 2016;44(8):e71. doi:10.1093/nar/gkv1507
17. Zhang Z, Hernandez K, Savage J, et al. Uniform genomic data analysis in the NCI Genomic Data Commons. *Nat Commun*. 2021;12(1):1226. doi:10.1038/s41467-021-21254-9
18. Alameer A, Chicco D. Chicco, geoCancerPrognosticDatasetsRetriever: a bioinformatics tool to easily identify cancer prognostic datasets on Gene Expression Omnibus (GEO). *Bioinformatics*. 2022;38(6):1761–1763. doi:10.1093/bioinformatics/btab852
19. Zheng H, Liu H, Li H. Characterization of stem cell landscape and identification of stemness-relevant prognostic gene signature to aid immunotherapy in colorectal cancer. *Stem Cell Res Ther*. 2022;13(1):244. doi:10.1186/s13287-022-02913-0
20. Liu Z, Liu L, Weng S, et al. BEST: a web application for comprehensive biomarker exploration on large-scale data in solid tumors. *J Big Data*. 2023;10(1):165. doi:10.1186/s40537-023-00844-y
21. Ke C, Dai S, Xu F, et al. Cuproptosis regulatory genes greatly contribute to clinical assessments of hepatocellular carcinoma. *BMC Cancer*. 2023;23(1):25. doi:10.1186/s12885-022-10461-2
22. Regan-Fendt K, Li D, Reyes R, et al. Transcriptomics-Based Drug Repurposing Approach Identifies Novel Drugs against Sorafenib-Resistant Hepatocellular Carcinoma. *Cancers (Basel)*. 2020;12(10):2730. doi:10.3390/cancers12102730
23. Huang D, Yuan W, Li H, Li S, Chen Z, Yang H. Identification of key pathways and biomarkers in sorafenib-resistant hepatocellular carcinoma using bioinformatics analysis. *Exp Ther Med*. 2018;16(3):1850–1858. doi:10.3892/etm.2018.6427
24. Tu X, Huang H, Xu S, Li C, Luo S. Single-cell transcriptomics reveals immune infiltrate in sepsis. *Front Pharmacol*. 2023;14:1133145. doi:10.3389/fphar.2023.1133145
25. Chi H, Zhao S, Yang J, et al. T-cell exhaustion signatures characterize the immune landscape and predict HCC prognosis via integrating single-cell RNA-seq and bulk RNA-sequencing. *Front Immunol*. 2023;14:1137025. doi:10.3389/fimmu.2023.1137025

26. Tang Q, Li W, Huang J, et al. Single-cell sequencing analysis of peripheral blood in patients with moyamoya disease. *Orphanet J Rare Dis*. 2023;18(1):174. doi:10.1186/s13023-023-02781-8
27. Chen C, Wang C, Pang R. Comprehensive single-cell transcriptomic and proteomic analysis reveals NK cell exhaustion and unique tumor cell evolutionary trajectory in non-keratinizing nasopharyngeal carcinoma. *J Transl Med*. 2023;21(1):278. doi:10.1186/s12967-023-04112-8
28. Tan Z, Chen X, Zuo J, Fu S, Wang H, Wang J. Comprehensive analysis of scRNA-Seq and bulk RNA-Seq reveals dynamic changes in the tumor immune microenvironment of bladder cancer and establishes a prognostic model. *J Transl Med*. 2023;21(1):223. doi:10.1186/s12967-023-04056-z
29. Alquicira-Hernandez J, Powell JE. Nebulosa recovers single-cell gene expression signals by kernel density estimation. *Bioinformatics*. 2021;37(16):2485–2487. doi:10.1093/bioinformatics/btab003
30. Chen B, Zhou X, Yang L, et al. A Cuproptosis Activation Scoring model predicts neoplasm-immunity interactions and personalized treatments in glioma. *Comput Biol Med*. 2022;148:105924. doi:10.1016/j.compbiomed.2022.105924
31. Gulati GS, Sikandar SS, Wesche DJ. Single-cell transcriptional diversity is a hallmark of developmental potential. *Science*. 2020;367(6476):405–411. doi:10.1126/science.aax0249
32. Ge LL, Wang ZC, Wei CJ, et al. Unraveling intratumoral complexity in metastatic dermatofibrosarcoma protuberans through single-cell RNA sequencing analysis. *Cancer Immunol Immunother*. 2023;72(12):4415–4429. doi:10.1007/s00262-023-03577-2
33. Wang G, Wu S, Xiong Z, Qu H, Fang X, Bao Y. CROST: a comprehensive repository of spatial transcriptomics. *Nucleic Acids Res*. 2024;52(D1):D882–d890. doi:10.1093/nar/gkad782
34. Aran D, Hu Z, Butte AJ. Butte, xCell: digitally portraying the tissue cellular heterogeneity landscape. *Genome Biol*. 2017;18(1):220. doi:10.1186/s13059-017-1349-1
35. Gene Ontology Consortium. Gene Ontology Consortium: going forward. *Nucleic Acids Res*. 2015;43(D1):D1049–1056. doi:10.1093/nar/gku1179
36. Wu B, Xi S. Bioinformatics analysis of differentially expressed genes and pathways in the development of cervical cancer. *BMC Cancer*. 2021;21(1):733. doi:10.1186/s12885-021-08412-4
37. Zhou Y, Zhou B, Pache L. Metascape provides a biologist-oriented resource for the analysis of systems-level datasets. *Nat Commun*. 2019;10(1):1523. doi:10.1038/s41467-019-09234-6
38. Kim B. Western Blot Techniques. *Methods Mol Biol*. 2017;1606:133–139.
39. Magaki S. An Introduction to the Performance of Immunohistochemistry. *Methods Mol Biol*. 2019;1897:289–298.
40. Im K, Mareninov S, Diaz MFP, Yong WH. An Introduction to Performing Immunofluorescence Staining. *Methods Mol Biol*. 2019;1897:299–311.
41. Luo H, Liu W, Zhou Y, Jiang X. Concentrated growth factor regulates the macrophage-mediated immune response. *Regen Biomater*. 2021;8(6):rbab049. doi:10.1093/rb/rbab049
42. Zhang Z, Wang Z-X, Chen Y-X. Integrated analysis of single-cell and bulk RNA sequencing data reveals a pan-cancer stemness signature predicting immunotherapy response. *Genome Med*. 2022;14(1):45. doi:10.1186/s13073-022-01050-w
43. Clevers H, Nusse R. Wnt/β-catenin signaling and disease. *Cell*. 2012;149(6):1192–1205. doi:10.1016/j.cell.2012.05.012
44. Hasbal-Celikok G, Aksoy-Sagirli P, Altiparmak-Ulbegi G, Can A. Identification of AKT1/β-catenin mutations conferring cetuximab and chemotherapeutic drug resistance in colorectal cancer treatment. *Oncol Lett*. 2021;21(3):209. doi:10.3892/ol.2021.12470
45. Isaacsson Velho P, Fu W, Wang H, Mirkheshti N. Wnt-pathway Activating Mutations Are Associated with Resistance to First-line Abiraterone and Enzalutamide in Castration-resistant Prostate Cancer. *Eur Urol*. 2020;77(1):14–21. doi:10.1016/j.eururo.2019.05.032
46. Belur Nagaraj A, Knarr M, Sekhar S, Connor RS, Joseph P, Kovalenko O. The miR-181a-SFRP4 Axis Regulates Wnt Activation to Drive Stemness and Platinum Resistance in Ovarian Cancer. *Cancer Res*. 2021;81(8):2044–2055. doi:10.1158/0008-5472.CAN-20-2041
47. Lehwald N, Tao GZ, Jang KY, Papandreou I. β-Catenin regulates hepatic mitochondrial function and energy balance in mice. *Gastroenterology*. 2012;143(3):754–764. doi:10.1053/j.gastro.2012.05.048
48. Liu Y, Sun Y, Guo Y. An Overview: the Diversified Role of Mitochondria in Cancer Metabolism. *Int J Biol Sci*. 2023;19(3):897–915. doi:10.7150/ijbs.81609
49. Eniafe J, Jiang S. The functional roles of TCA cycle metabolites in cancer. *Oncogene*. 2021;40(19):3351–3363. doi:10.1038/s41388-020-01639-8
50. Bassot A, Chen J, Takahashi-Yamashiro K, et al. The endoplasmic reticulum kinase PERK interacts with the oxidoreductase ERO1 to metabolically adapt mitochondria. *Cell Rep*. 2023;42(1):111899. doi:10.1016/j.celrep.2022.111899
51. Clara JA, Monge C, Yang Y, Takebe N. Targeting signalling pathways and the immune microenvironment of cancer stem cells - A clinical update. *Nat Rev Clin Oncol*. 2020;17(4):204–232. doi:10.1038/s41571-019-0293-2
52. Noe JT, Mitchell RA. MIF-Dependent Control of Tumor Immunity. *Front Immunol*. 2020;11:609948. doi:10.3389/fimmu.2020.609948
53. Hiramatsu N, Tago T, Satoh T, Satoh AK. ER membrane protein complex is required for the insertions of late-synthesized transmembrane helices of Rh1 in Drosophila photoreceptors. *Mol Biol Cell*. 2019;30(23):2890–2900. doi:10.1091/mbc.E19-08-0434
54. Wu H, Smalinskaitė L, Hegde RS. EMC rectifies the topology of multipass membrane proteins. *Nat Struct Mol Biol*. 2024;31(1):32–41. doi:10.1038/s41594-023-01120-6
55. Cournia Z, Allen TW, Andricioaei I, et al. Membrane Protein Structure, Function, and Dynamics: a Perspective from Experiments and Theory. *J Membr Biol*. 2015;248(4):611–640. doi:10.1007/s00232-015-9802-0
56. Chen X, Cubillos-Ruiz JR. Endoplasmic reticulum stress signals in the tumour and its microenvironment. *Nat Rev Cancer*. 2021;21(2):71–88. doi:10.1038/s41568-020-00312-2
57. Oakes SA. Endoplasmic Reticulum Stress Signaling in Cancer Cells. *Am J Pathol*. 2020;190(5):934–946. doi:10.1016/j.ajpath.2020.01.010
58. Akiyama T. Wnt/beta-catenin signaling. *Cytokine Growth Factor Rev*. 2000;11(4):273–282. doi:10.1016/S1359-6101(00)00011-3
59. Fujikura K, Akita M, Ajiki T, Fukumoto T, Itoh T, Zen Y. Recurrent Mutations in APC and CTNNB1 and Activated Wnt/β-catenin Signaling in Intraductal Papillary Neoplasms of the Bile Duct: a Whole Exome Sequencing Study. *Am J Surg Pathol*. 2018;42(12):1674–1685. doi:10.1097/PAS.0000000000001155
60. Perugorria MJ, Olaizola P, Labiano I, et al. Wnt-β-catenin signalling in liver development, health and disease. *Nat Rev Gastroenterol Hepatol*. 2019;16:121–136.
61. Leung HW. EPHB2 Activates β-Catenin to Enhance Cancer Stem Cell Properties and Drive Sorafenib Resistance in Hepatocellular Carcinoma. *Cancer Res*. 2021;81(12):3229–3240. doi:10.1158/0008-5472.CAN-21-0184
62. Najafi M, Mortezaee K, Majidpoor J. Cancer stem cell (CSC) resistance drivers. *Life Sci*. 2019;234:116781. doi:10.1016/j.lfs.2019.116781

63. Kudo M, Finn RS, Qin S, et al. Lenvatinib versus sorafenib in first-line treatment of patients with unresectable hepatocellular carcinoma: a randomised phase 3 non-inferiority trial. *Lancet*. 2018;391:1163–1173.
64. Qin S, Bi F, Gu S, Bai Y. Donafenib Versus Sorafenib in First-Line Treatment of Unresectable or Metastatic Hepatocellular Carcinoma: a Randomized, Open-Label, Parallel-Controlled Phase II-III Trial. *J Clin Oncol*. 2021;39(27):3002–3011. doi:10.1200/JCO.21.00163
65. Tang W, Chen Z, Zhang W, et al. The mechanisms of sorafenib resistance in hepatocellular carcinoma: theoretical basis and therapeutic aspects. *Signal Trans Targ Ther*. 2020;5(1):87. doi:10.1038/s41392-020-0187-x
66. Tanabe A, Sahara H. The Metabolic Heterogeneity and Flexibility of Cancer Stem Cells. *Cancers*. 2020;12(10):2780. doi:10.3390/cancers12102780
67. Yasuda T, Ishimoto T, Baba H. Conflicting metabolic alterations in cancer stem cells and regulation by the stromal niche. *Regen Ther*. 2021;17:8–12. doi:10.1016/j.reth.2021.01.005
68. Tanabe S, Quader S, Cabral H, Ono R. Interplay of EMT and CSC in Cancer and the Potential Therapeutic Strategies. *Front Pharmacol*. 2020;11:904. doi:10.3389/fphar.2020.00904
69. Lee SY, Jeong EK, Ju MK, Jeon HM, Kim MY. Induction of metastasis, cancer stem cell phenotype, and oncogenic metabolism in cancer cells by ionizing radiation. *Mol Cancer*. 2017;16(1):10. doi:10.1186/s12943-016-0577-4
70. Park K, Veena MS, Shin DS. Key Players of the Immunosuppressive Tumor Microenvironment and Emerging Therapeutic Strategies. *Front Cell Dev Biol*. 2022;10:830208. doi:10.3389/fcell.2022.830208
71. Allavena P, Digifico E, Belgiovine C. Macrophages and cancer stem cells: a malevolent alliance. *Mol Med*. 2021;27(1):121. doi:10.1186/s10020-021-00383-3
72. Zhao Q, Zong H, Zhu P, et al. Crosstalk between colorectal CSCs and immune cells in tumorigenesis, and strategies for targeting colorectal CSCs. *Exp Hematol Oncol*. 2024;13:6.
73. Wang S. Targeting M2-like tumor-associated macrophages is a potential therapeutic approach to overcome antitumor drug resistance. *npj Precision Oncology*. 2024;8:31.
74. Yang YI, Wang YY, Ahn JH, Kim BH, Choi JH. CCL2 overexpression is associated with paclitaxel resistance in ovarian cancer cells via autocrine signaling and macrophage recruitment. *Biomed Pharmacother*. 2022;153:113474. doi:10.1016/j.biopha.2022.113474
75. Xiao M, He J, Yin L, Chen X, Zu X, Shen Y. Tumor-Associated Macrophages: critical Players in Drug Resistance of Breast Cancer. *Front Immunol*. 2021;12:799428. doi:10.3389/fimmu.2021.799428
76. Chen S, Du Y, Guan XY, Yan Q. The current status of tumor microenvironment and cancer stem cells in sorafenib resistance of hepatocellular carcinoma. *Front Oncol*. 2023;13:1204513. doi:10.3389/fonc.2023.1204513
77. Li J, Liu Y, Zheng R, Qu C, Li J. Molecular mechanisms of TACE refractoriness: directions for improvement of the TACE procedure. *Life Sci*. 2024;342:122540. doi:10.1016/j.lfs.2024.122540
78. Minici R, Siciliano MA, Ammendola M, Santoro RC, Barbieri V. Prognostic Role of Neutrophil-to-Lymphocyte Ratio (NLR), Lymphocyte-to-Monocyte Ratio (LMR), Platelet-to-Lymphocyte Ratio (PLR) and Lymphocyte-to-C Reactive Protein Ratio (LCR) in Patients with Hepatocellular Carcinoma (HCC) undergoing Chemoembolizations (TACE) of the Liver: the Unexplored Corner Linking Tumor Microenvironment, Biomarkers and Interventional Radiology. *Cancers*. 2022;15:1.